Science Advances
AAAS

advances.sciencemag.org/cgi/content/full/4/4/eaat1098/DC1

# Supplementary Materials for

## Experimental signatures of spin superfluid ground state in canted antiferromagnet $Cr_2O_3$ via nonlocal spin transport

Wei Yuan, Qiong Zhu, Tang Su, Yunyan Yao, Wenyu Xing, Yangyang Chen, Yang Ma, Xi Lin, Jing Shi, Ryuichi Shindou, X. C. Xie, Wei Han

Published 13 April 2018, *Sci. Adv.* **4**, eaat1098 (2018)
DOI: 10.1126/sciadv.aat1098

**This PDF file includes:**

**section S1. First and second harmonic results on (0001)-oriented $Cr_2O_3$ thin film**

During nonlocal spin transport measurements, two lock-in amplifiers are used to probe the first and second harmonic voltages. The first harmonic resistance ( $R_{1\varpi}$ ) is calculated from the first harmonic voltage ( $V_{1\varpi}$ ) based on the equation: $R_{1\varpi} = V_{1\varpi} / I_{AC}$. And the second harmonic resistance ( $R_{2\varpi}$ ) is calculated from the second harmonic voltage ( $V_{2\varpi}$ ) based on the equation: $R_{2\varpi} = \sqrt{2}V_{2\varpi} / I_{AC}{}^2$. Figure S4 shows the typical results measured on two devices ($d$ = 10 μm and 2 μm) at $B$ = 9 T and $T$ = 2 K. For both devices, the second harmonic resistances could be clearly observed, which follow a sin ($\varphi$) relationship as a function of the magnetic field angle (*25*). Whileas, no obvious first harmonic signal is observed within a noise level of 0.05 mΩ.

This observation could be attributed to that the spin injection efficiency by thermal means is much higher than that via spin Hall effect, which is not surprising since it has already been observed in previous studies of spin injection from Pt to ferromagnetic insulators (*30, 31*). Nevertheless, to fully understand the absence of the first harmonic nonlocal spin signal, further theoretical and experimental studies are needed.

**section S2. Comparison of low-temperature and high-temperature results on (0001)-oriented $Cr_2O_3$ thin film**

The low temperature spin transport via spin superfluid ground state has exhibited two major differences compared to the high temperature spin transport via incoherent magnons, as discussed below.

The first major difference is contrasting spacing dependence of the nonlocal spin signal. As stated in the main text, the nonlocal signal decays quite slowly and quantitatively agrees well with the spin superfluid model: $R_{NL} = R_{NL}^{d=0} \frac{L_\alpha}{d + L_\alpha}$ (*22*). At high temperatures, the nonlocal spin signal decays rapidly as the spacing increases. As shown in fig. S5A, as the spacing increases,

the nonlocal spin signal follows a relationship of $R_{NL} \sim \frac{\exp(d/\lambda)}{1-\exp(2d/\lambda)} \sim \frac{1}{d}$ (when *d* is smaller than the magnon diffusion length ($\lambda$)). This feature is the similar to the diffusion of thermally-generated incoherent magnons in YIG (*25, 30*). The transition from spin superfluid transport to thermally-generated incoherent magnon transport can also be evidenced from the rapid decrease of $L_\alpha$ as the temperature increases above ~ 20 K. When the spacing is larger than $L_\alpha$, the damping is very critical to forbidden the long range spin superfluid transport (*22*).

Besides, the current dependence of the nonlocal spin signals are different for low and high temperatures, as shown in fig. S6. For low temperature results at 2 and 10 K, a critical current is observed, as indicated in fig. S6B. However, for the nonlocal spin transport at 80 K, $V_{2\varpi}$ is linearly proportional to $I_{AC}^{\ 2}$ without a critical current density (fig. S6D). The critical current observed at low temperatures for the spin superfluid ground state could be attributed to the critical spin torque that is needed to overcome the anisotropy energy to make the canted spins rotate along the magnetic field direction. As discussed in previous theoretical studies that the anisotropy in antiferromagnet defines a critical spin current density at the injector to overcome the antiferromagnet pining (*22*).

**section S3. Mechanism for the modest enhancement of the nonlocal spin signal at ~60 K**

The modest enhancement of the nonlocal spin signal on the ~ 19 nm (0001)-oriented thin film is observed at ~ 60 K. To our best knowledge, it could be due to two mechanisms inferred from previous studies. The first one is due to the large spin fluctuation near the Neel temperature of the $Cr_2O_3$ thin film (*27, 29, 35*). And the second one is related to magnon-phonon drag effect (*36, 37*). To probe the mechanism, we experimentally measure the Neel temperature of the ~19 nm $Cr_2O_3$ thin film via exchange bias and its thermal conductivity via the 3ω method (*38, 39*). fig. S7 shows the exchange bias between the 2 nm Py and $Cr_2O_3$ thin films as a function of the temperature. A blocking temperature of ~ 260 K is observed, which ruled out the mechanism of large spin fluctuation to account for our observation. For the thermal conductivity measurements on the (0001)-oriented $Cr_2O_3$ bulk single crystal and ~19 nm thin films, a typical device is shown

in fig. S8A, where the electrodes are made of Pt. The thermal conductivity results of the bulk $Cr_2O_3$ (fig. S8B) are similar to the previous study using the heat capacity method (*24*). Figure S8C shows the thermal conductivity of the ~ 19 nm thin film as a function of the temperature. A modest peak is observed at ~ 70 K. It seems that that the magnon-phonon coupling could be the possible cause for the modest enhancement of the nonlocal spin signal at ~ 60 K. However, to fully understand this high temperature modest enhancement, further theoretical and experimental investigations would be essential.

**section S4. Supporting results on extra samples: 6- and 45-nm (0001)-oriented $Cr_2O_3$ films**

Extra samples are measured to further confirm the spin transport via spin superfluid ground state probed on the ~19 nm (0001)-oriented $Cr_2O_3$ film. Figures S9 and S10 show the nonlocal spin transport results measured on the ~ 6 nm and ~ 45 nm (0001)-oriented $Cr_2O_3$ films, respectively. Similar to ~19 nm (0001)-oriented $Cr_2O_3$ film, the rapid enhancement and saturation of the nonlocal spin signal at low temperatures are observed (figs. S9A and S10A), consistent with theoretical predications (*15*). At low temperatures, the slow decaying of the spin signal as the spacing increases (figs. S9B and S10B), which is consistent with the spin transport via spin superfluid model (*22*). Besides, as the temperature increases, the transition from spin superfluid transport to thermally-generated incoherent magnon diffusion is observed (figs. S9C, S9D, S10C, and S10D), similar to the results on ~19 nm (0001)-oriented $Cr_2O_3$ film.

Figure S11 shows the nonlocal spin signal measured on all the (0001)-oriented $Cr_2O_3$ films with various thicknesses. The nonlocal spin signal is larger for thicker films, which is due to higher spin superfluid densities in thicker films.

**section S5. First and second harmonic results on (11$\bar{2}$0)-oriented $Cr_2O_3$ thin film**

Figure S12 shows the typical results measured on two devices fabricated on the ~ 18 nm (11-20)-oriented $Cr_2O_3$ thin film ($d$ = 10 and 2 μm) at $B$ = 9 T and $T$ = 2 K. For both devices, the second harmonic resistances could be clearly observed, which follow a sin ($\varphi$) relationship as a function

of the magnetic field angle. Whileas, no obvious first harmonic signal is observed within a noise level of 0.02 mΩ. This observation is similar to the results on (0001)-oriented $Cr_2O_3$ thin films.

**section S6. Temperature and spacing dependence of the nonlocal spin transport on (11$\bar{2}$0)-oriented $Cr_2O_3$ thin film**

Figure S13 shows the nonlocal spin transport results measured on the ~ 18 nm (11$\bar{2}$0)-oriented $Cr_2O_3$ thin film at $B$ = 9 T. The rapid enhancement and saturation of the nonlocal spin signal at low temperatures are observed (fig. S13A), which is consistent with the spin superfluid transport expected theoretically (*15*). The spacing dependence of the nonlocal spin signal at $T$ = 2 and 10 K (fig. S13B) is also consistent with the spin superfluid model (red dashed lines) (*22*), but very different from the exponential decaying expected for thermally-generated incoherent magnons (green dashed lines).

Different from the low temperature spin transport via spin superfluid, the spin transport via incoherent magnons is observed at high temperatures (fig. S13C). The transition from spin superfluid transport to thermally-generated incoherent magnon transport can also be evidenced from the rapid decrease of $L_\alpha$ as the temperature increases (fig. S13D). Besides, the current dependence of the nonlocal spin signals are also different at low and high temperatures, as shown in fig. S14. For low temperature results at 2 and 10 K, a critical current is observed (fig. S14A and S14B). This is different from the nonlocal spin transport at 80 K (fig. S14C and S14D) with no signatures of critical current.

**section S7. Magnetic field dependence of the nonlocal spin transport on (0001)-oriented $Cr_2O_3$ thin film**

The role of canted angle for the spin transport in the spin superfluid state is studied for the ~ 19 nm (0001)-oriented $Cr_2O_3$ film. The canted angles can be controlled by the magnetic field strength. Figure S15A shows the nonlocal vs. the magnetic field angle under 1, 3, 5, 7, and 9 T on the nonlocal device ($d$ = 10 μm) at 2 K. These magnetic fields give rise to very tiny canted angles since they are significantly smaller compared to the saturation magnetic field. The

nonlocal spin signal exhibits a linear relationship vs. the in-plane magnetic field (fig. S15B). This is because the total spin polarization at the detector is proportional to the product of the spin superfluid density and the field-induced canted magnetization along $x$ direction ($m_x$). For all of the magnetic fields from 1 T to 9 T, the nonlocal spin signal exhibits similar features (fig. S15C), including the large enhancement from ~ 20 K, and the saturation when the temperature is below ~ 5 K. To study temperature dependence of the spin superfluid density, we normalize the nonlocal spin signal by the value at 2 K (fig. S15D). The normalized nonlocal spin signals for all the magnetic fields almost fall on the same curve, indicating a negligible effect of the magnetic field strength on the saturated spin density for the spin superfluid ground state.

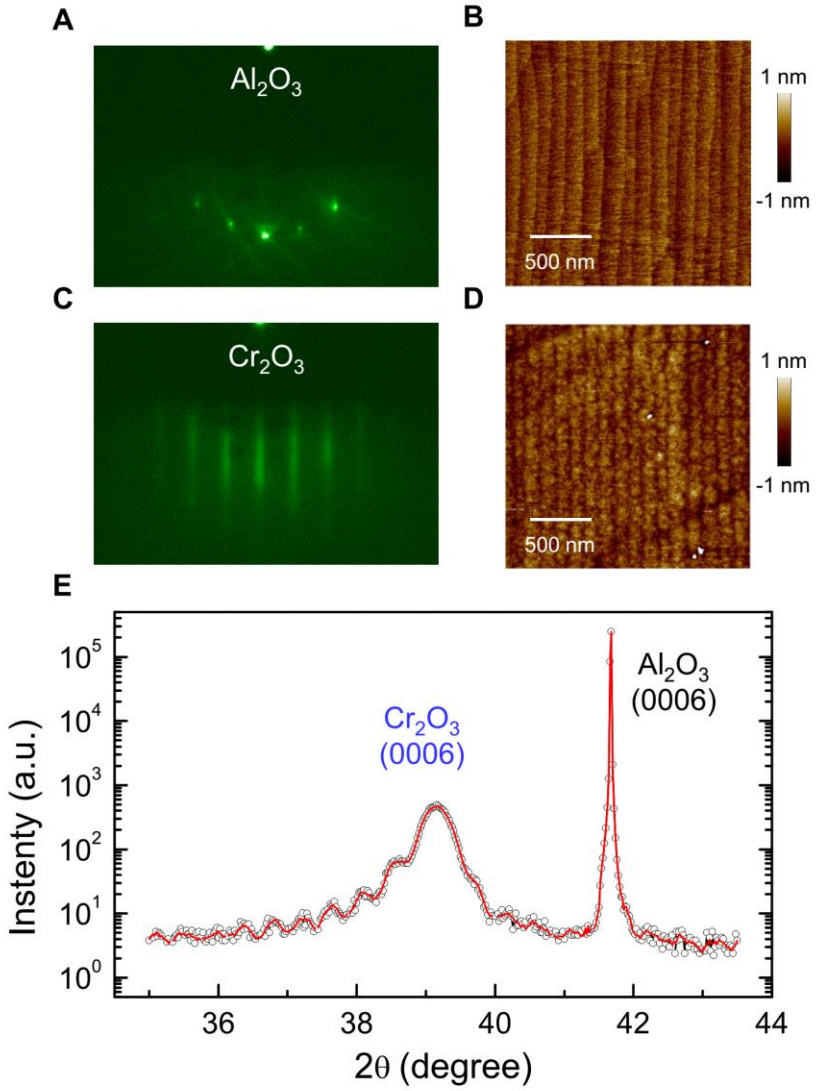


**fig. S1. RHEED and XRD of the (0001)-oriented $Cr_2O_3$ thin film (~19 nm) on the (0001)-oriented $Al_2O_3$ substrate.** (**A-D**) RHEED patterns and the AFM results of the (0001)-oriented $Al_2O_3$ substrate and the ~ 19 nm epitaxial (0001)-oriented $Cr_2O_3$ thin film. The width of the atomic steps is ~ 100 nm. (**E**) High resolution XRD pattern of the ~ 19 nm epitaxial (0001)-oriented $Cr_2O_3$ thin film on the $Al_2O_3$ substrate. The thickness of $Cr_2O_3$ thin film could be determined by the fitting curve (red line).

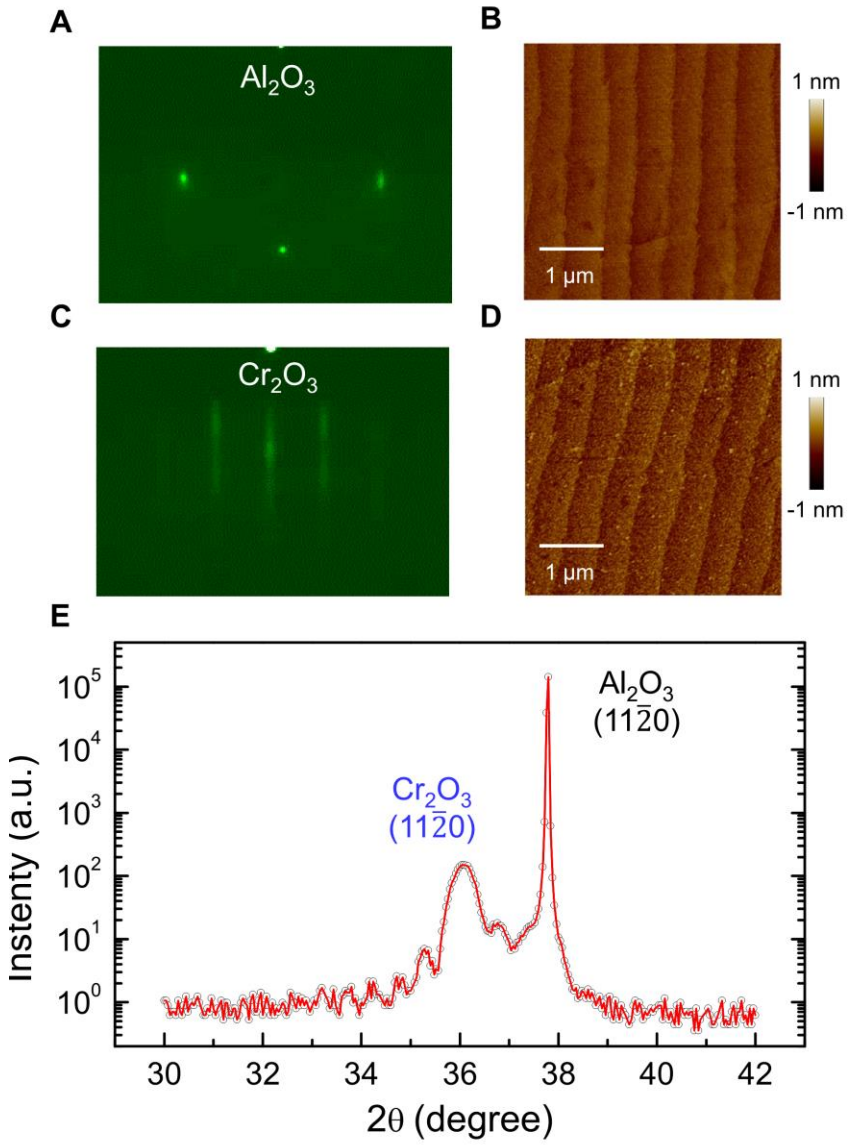


**fig. S2. RHEED and XRD of the $(11\bar{2}0)$-oriented $Cr_2O_3$ thin film (~18 nm) on the $(11\bar{2}0)$-oriented $Al_2O_3$ substrate.** (**A-D**) RHEED patterns and the AFM results of the $(11\bar{2}0)$-oriented $Al_2O_3$ substrate and the ~ 18 nm epitaxial $(11\bar{2}0)$-oriented $Cr_2O_3$ thin film. The width of the atomic steps is ~ 1.0 μm. (**E**) High resolution XRD pattern of the ~ 18 nm epitaxial $(11\bar{2}0)$-oriented $Cr_2O_3$ thin film on the $Al_2O_3$ substrate. The thickness of $Cr_2O_3$ thin film could be determined by the fitting curve (red line).

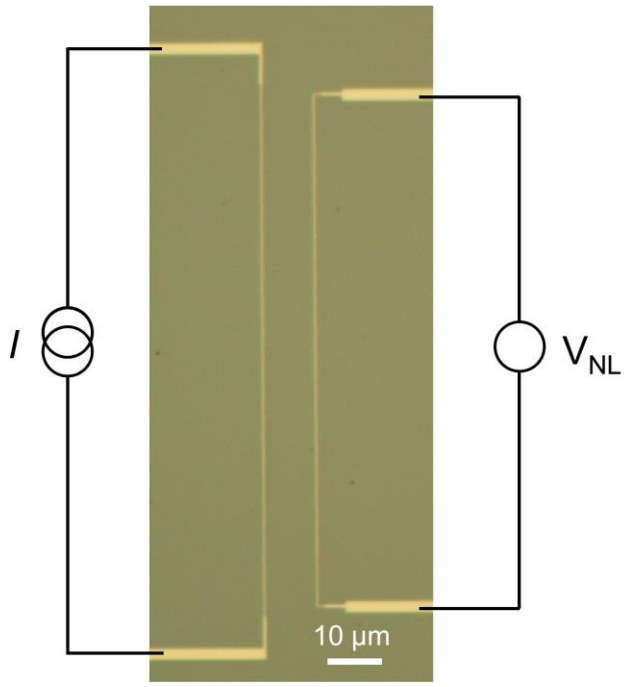


**fig. S3. The typical optical image of the nonlocal device and the nonlocal measurement.** The thickness of the (0001)-oriented $Cr_2O_3$ is ~ 19 nm, and the spacing between two Pt strips (the spin injector and detector) is 10 μm. The nonlocal spin signal is measured in the nonlocal geometry with standard low frequency lock-in technique.

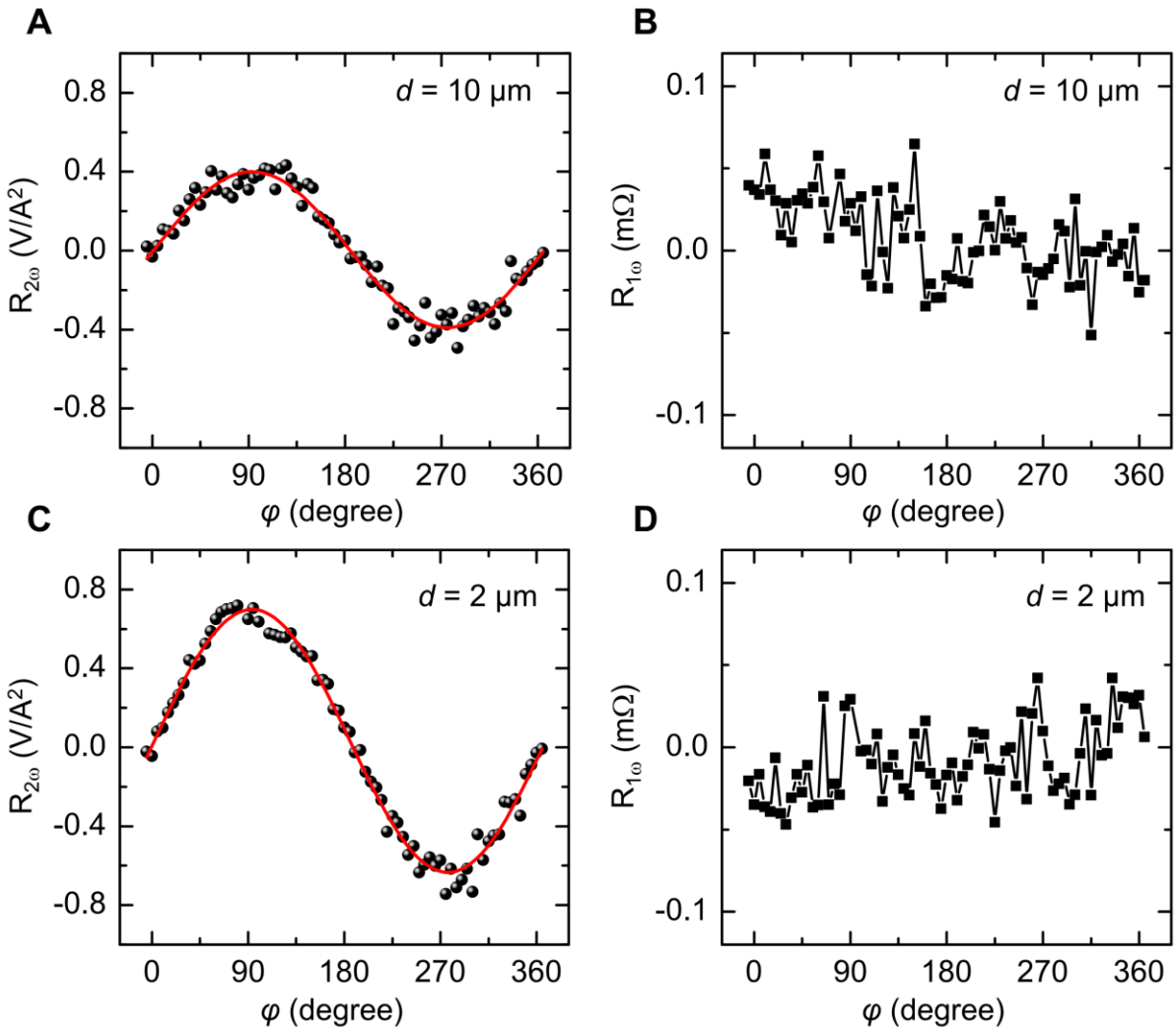


**fig. S4. The first and second harmonic nonlocal resistance on the ~19-nm (0001)-oriented $Cr_2O_3$ film.** (**A-B**) The first and second harmonic nonlocal resistance for the device of $d$ = 10 μm at $B$ = 9 T and $T$ = 2 K. (**C-D**) The first and second harmonic nonlocal resistance for the device of $d$ = 2 μm at $B$ = 9 T and $T$ = 2 K. The second harmonic nonlocal resistance is proportional to sin ($\varphi$), indicated by red lines in A and C. No clear first harmonic nonlocal spin signal is observed for both devices.

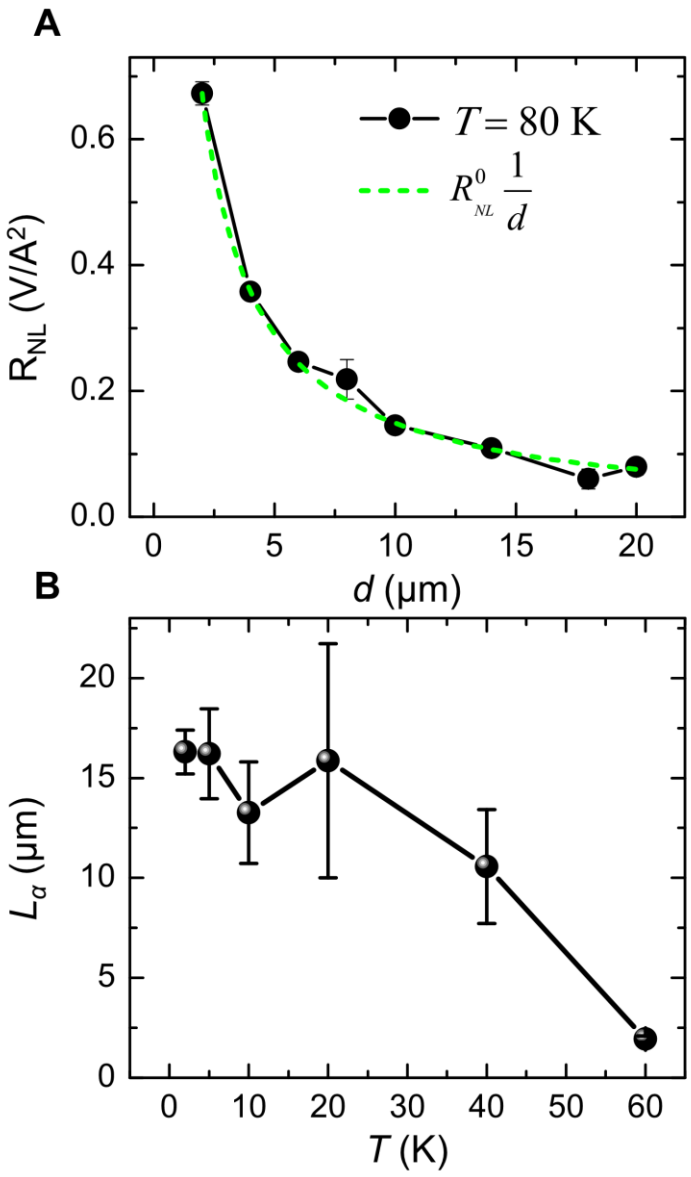


**fig. S5. The transition from spin transport via spin superfluid to that via thermally generated incoherent magnons.** (**A**) The spacing dependence of the nonlocal spin signal at 80 K obtained on the ~ 19 nm (0001)-oriented $Cr_2O_3$ film. The green dashed line is the fitting curve based on the incoherent magnon diffusion model ( $R_{NL} \sim \frac{1}{d}$ ). (**B**) The temperature dependence of $L_\alpha$ obtained based on the spin superfluid transport model ( $R_{NL} \sim \frac{1}{d + L_\alpha}$ ).

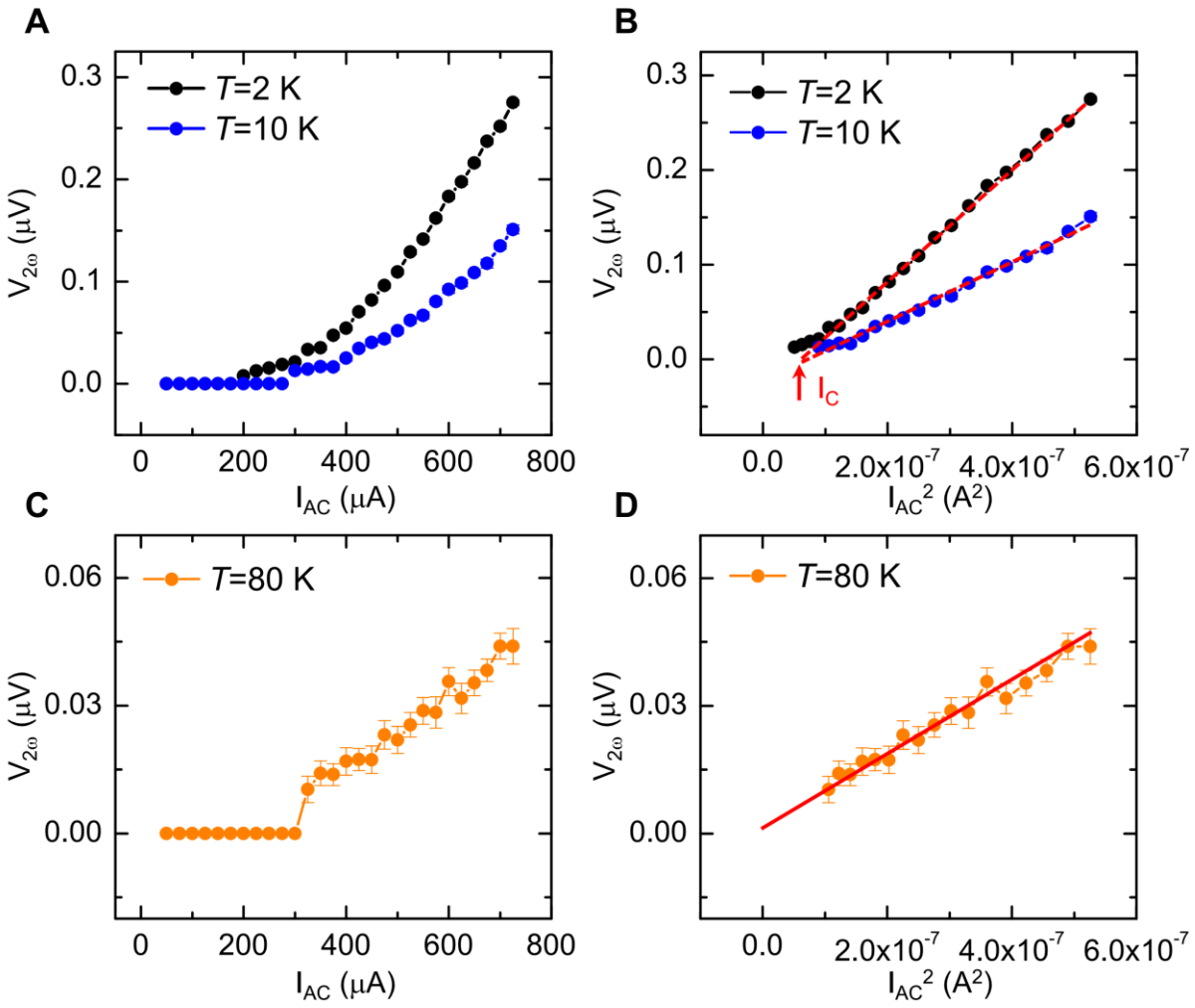


**fig. S6. Current dependence of the nonlocal spin transport on the ~19-nm (0001)-oriented $Cr_2O_3$ film.** (**A-B**) The second harmonic spin voltage vs. $I$ and $I^2$ at $T$ = 2 and 10 K and $B$ = 9 T on the device with $d$ = 10 μm. A critical current ($I_C$) is observed, which is needed to overcome uniaxial anisotropy to induce the spin superfluid transport. (**C-D**) The second harmonic spin voltage vs. $I$ and $I^2$ at $T$ = 80 K and $B$ = 9 T on the device with $d$ = 10 μm. The second harmonic voltage is proportional to $I^2$ without a critical current.

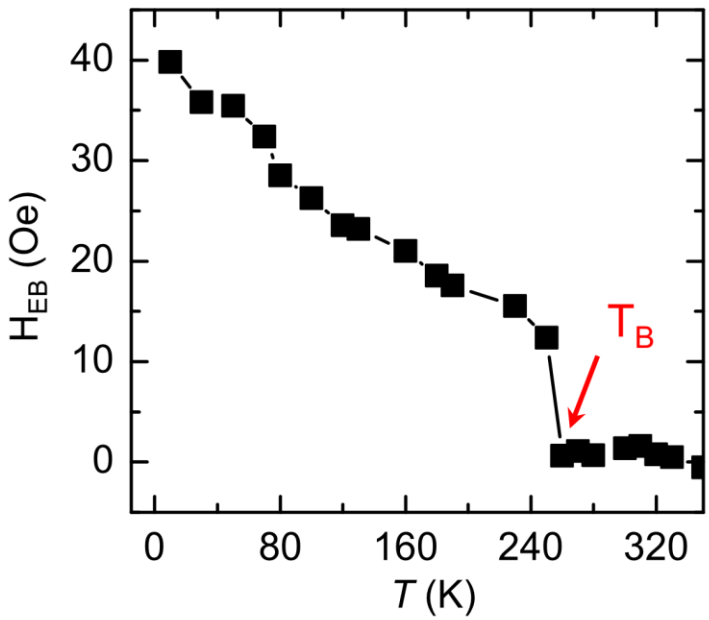


**fig. S7. The exchange bias between 2-nm Py and the ~19-nm (0001)-oriented film.** The blocking temperature is ~ 260 K.

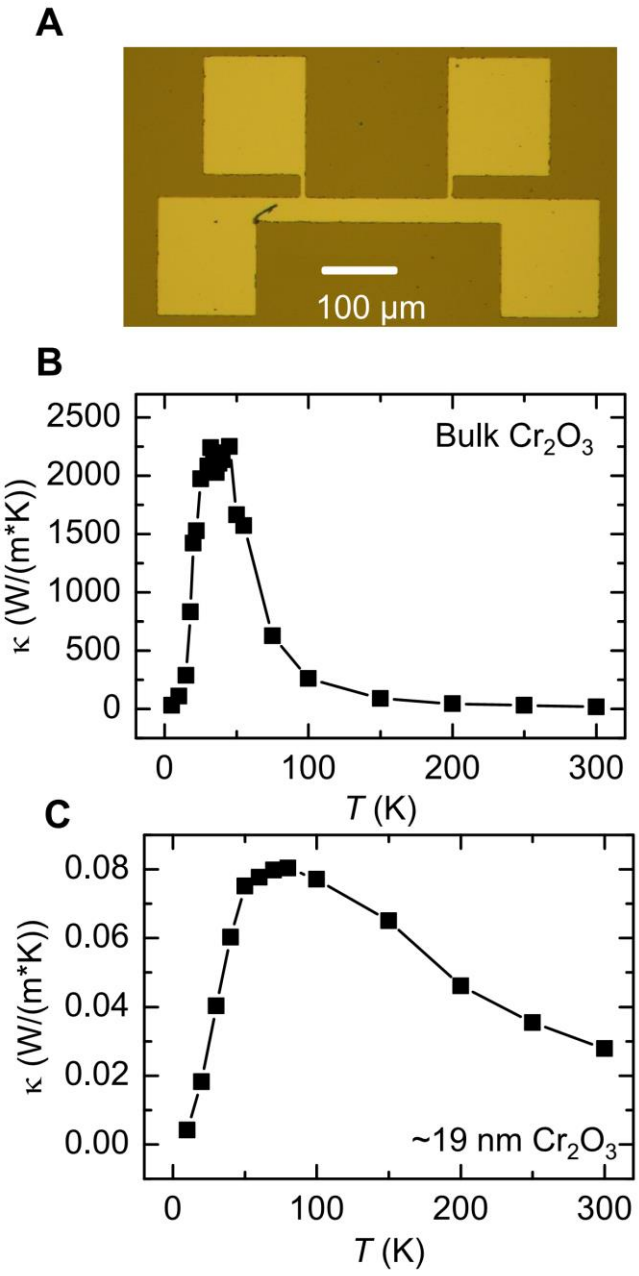


**fig. S8. Thermal conductivity (κ) measured by the 3ω method for the (0001)-oriented $Cr_2O_3$ film.** (**A**) The optical image of the device fabricated on the film, where the Pt width is 40 μm. (**B-C**) The thermal conductivity of a single crystal of (0001)-oriented bulk $Cr_2O_3$ crystal and the ~ 19 nm $Cr_2O_3$ film, respectively.

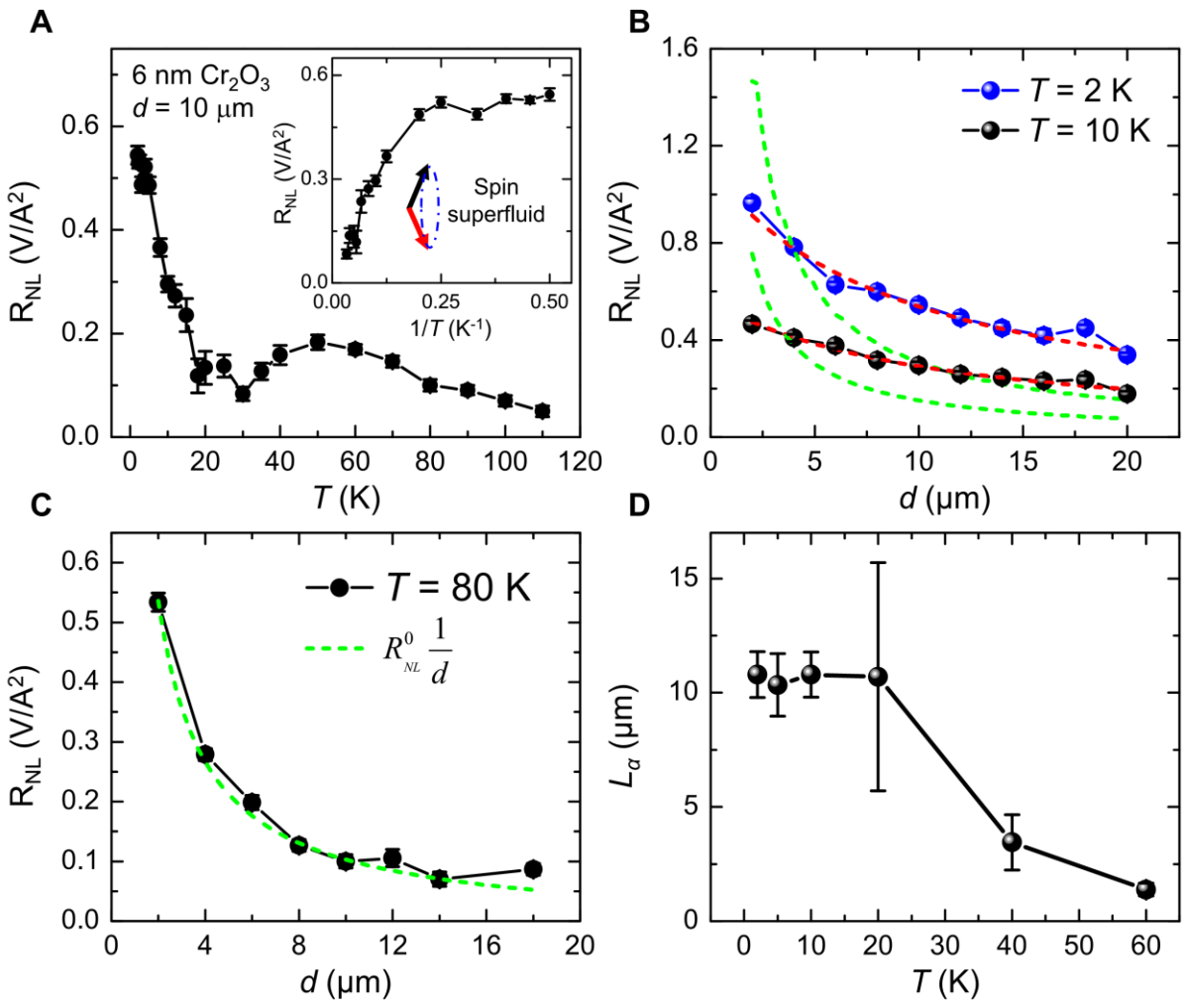


**fig. S9. The nonlocal spin transport on the ~6-nm (0001)-oriented $Cr_2O_3$ film.** (**A**) The temperature dependence of the nonlocal spin signal for the device with $d$ = 10 μm. Inset: The nonlocal spin signal as a function of 1/$T$. (**B-C**) The spacing dependence of the nonlocal spin signal at $T$ = 2 K, 10, and 80 K. The red dashed lines are the fitting curves based on spin superfluid model ( $R_{NL} \sim \frac{1}{d + L_\alpha}$ ), and the green dashed lines are fitting curves based on the incoherent magnon diffusion model ( $R_{NL} \sim \frac{1}{d}$ ). (**D**) The temperature dependence of $L_\alpha$ obtained based on the spin superfluid transport model.

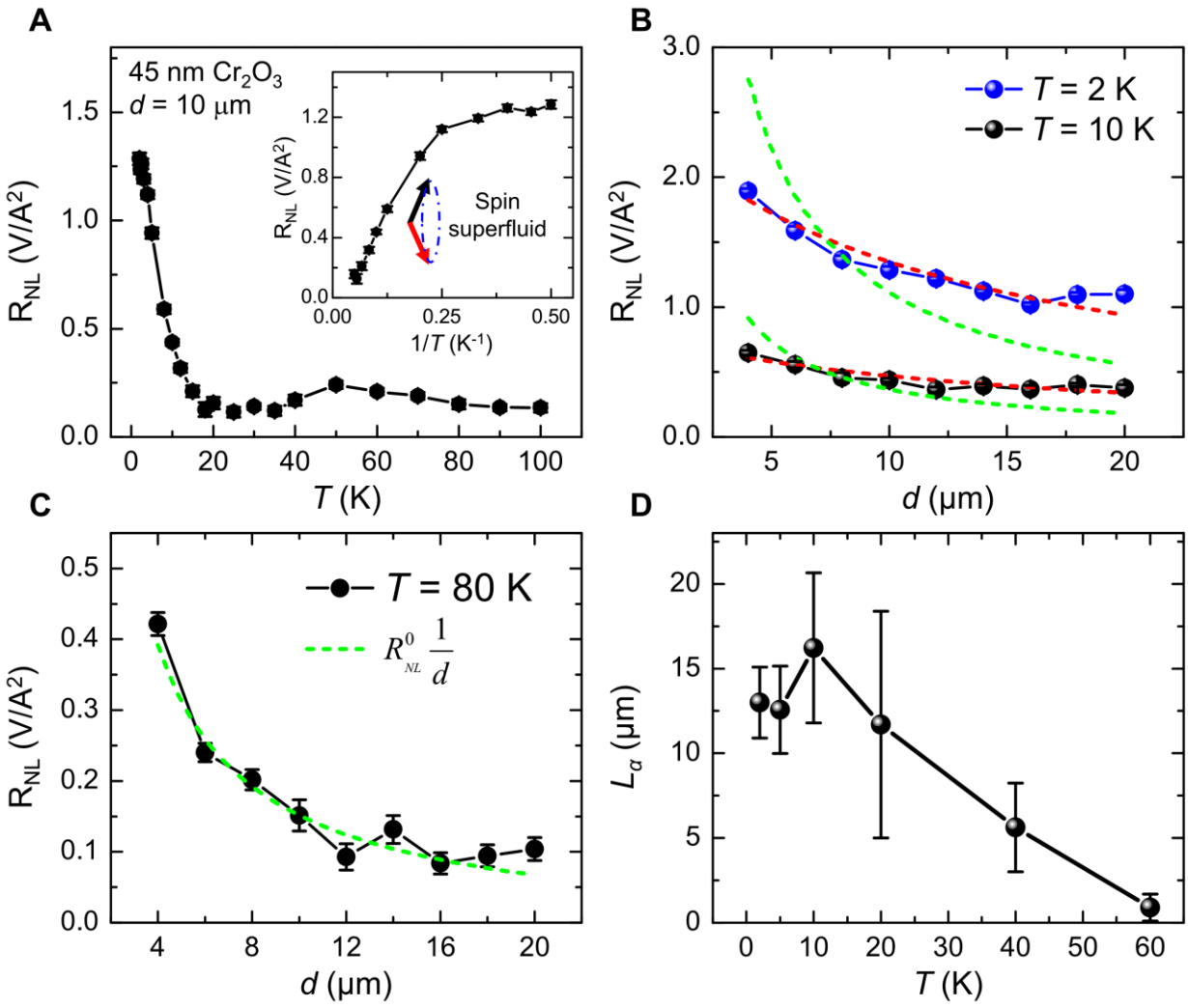


**fig. S10. The nonlocal spin transport on the ~45-nm (0001)-oriented $Cr_2O_3$ film. (A)** The temperature dependence of the nonlocal spin signal for the device with $d$ = 10 μm. Inset: The nonlocal spin signal as a function of 1/$T$. (**B-C**) The spacing dependence of the nonlocal spin signal at $T$ = 2 K, 10, and 80 K. The red dashed lines are the fitting curves based on spin superfluid model ( $R_{NL} \sim \frac{1}{d + L_\alpha}$ ), and the green dashed lines are fitting curves based on the incoherent magnon diffusion model ( $R_{NL} \sim \frac{1}{d}$ ). (**D**) The temperature dependence of $L_\alpha$ obtained based on the spin superfluid transport model.

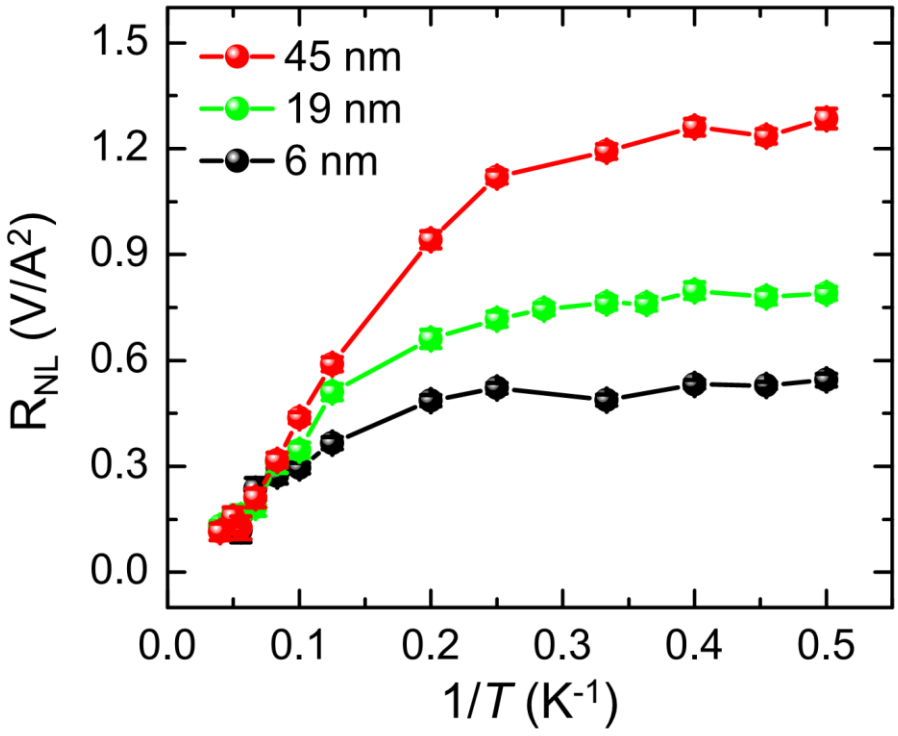


**fig. S11. Temperature dependence of the nonlocal spin transport for (0001)-oriented $Cr_2O_3$ films with various thicknesses.** $R_{nonlocal}$ vs. $1/T$ for the $d$ = 10 μm devices fabricated on 6 nm, 19 nm, and 45 nm thick (0001)-oriented $Cr_2O_3$ films at $B$ = 9 T.

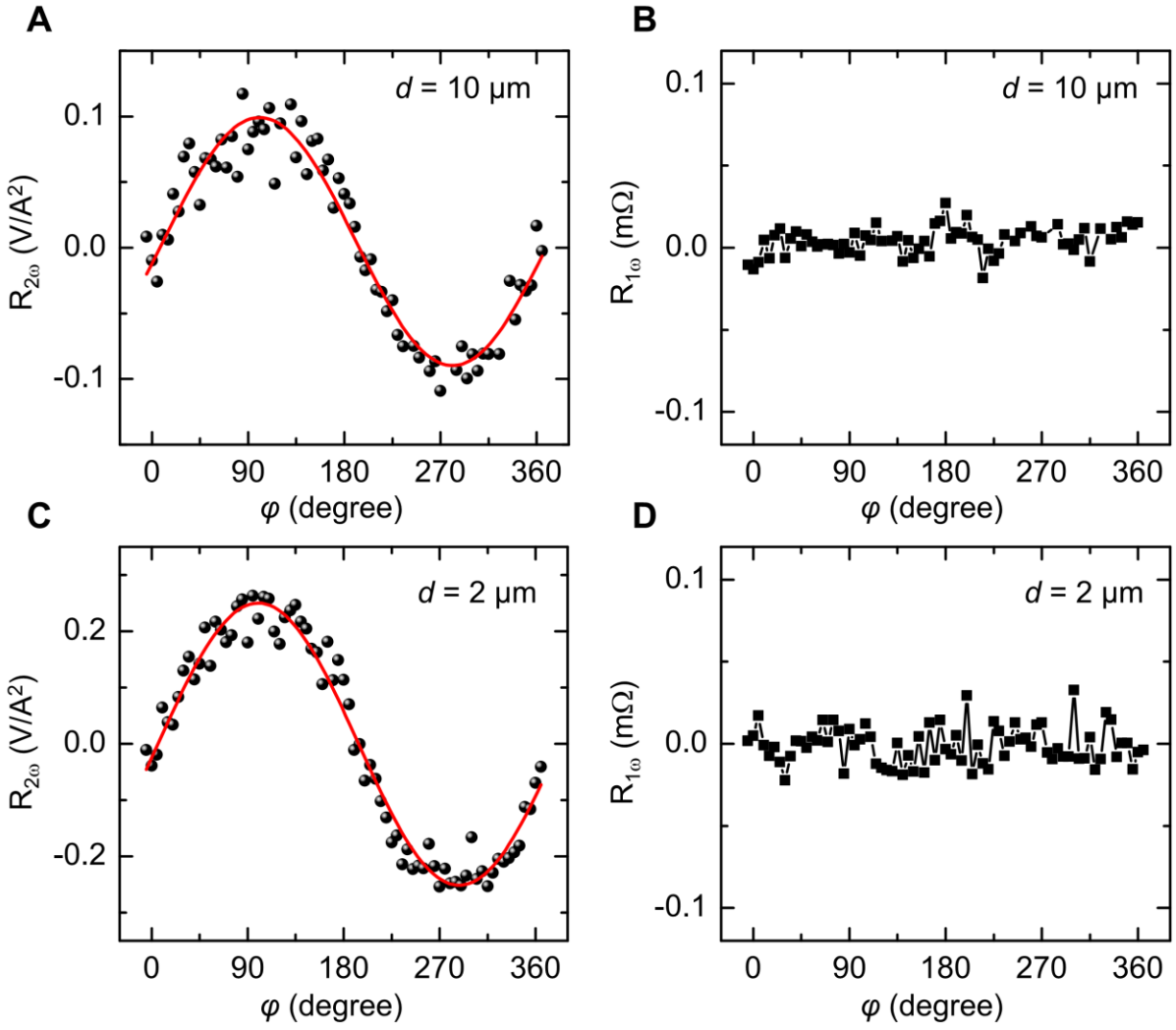


**fig. S12. The first and second harmonic nonlocal resistance on the ~18-nm (11$\bar{2}$0)-oriented $Cr_2O_3$ film.** (**A-B**) The first and second harmonic nonlocal resistance for the device of $d$ = 10 μm at $B$ = 9 T and $T$ = 2 K. (**C-D**) The first and second harmonic nonlocal resistance for the device of $d$ = 2 μm at $B$ = 9 T and $T$ = 2 K. The second harmonic nonlocal resistance is proportional to sin ($\varphi$), indicated by red lines in A and C. No clear first harmonic nonlocal spin signal is observed for both devices.

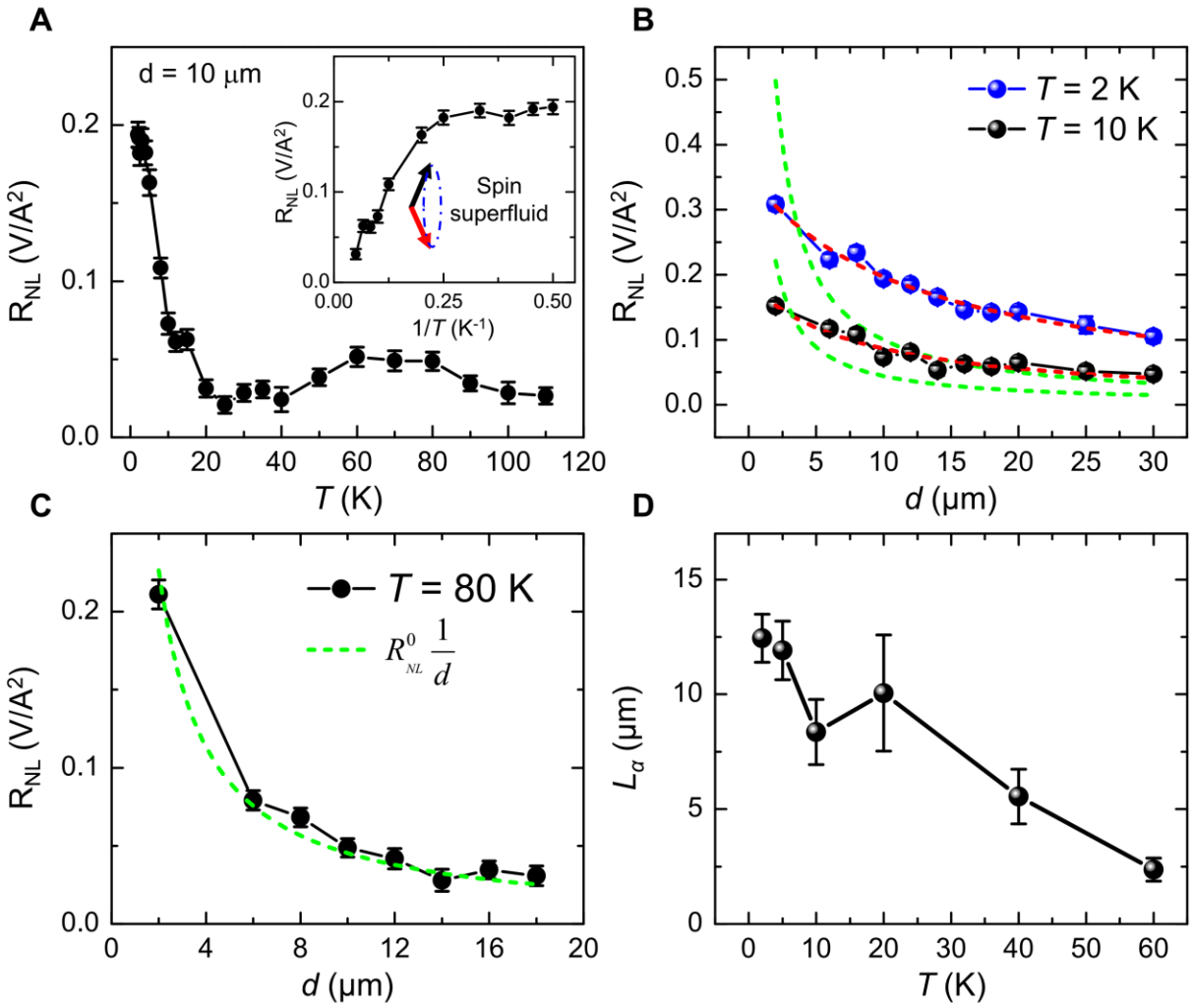


**fig. S13. The nonlocal spin transport on the ~18-nm (11$\bar{2}$0)-oriented $Cr_2O_3$ film.** (**A**) The temperature dependence of the nonlocal spin signal for the device with $d$ = 10 μm at $B$ = 9 T. Inset: The nonlocal spin signal as a function of 1/$T$. (**B-C**) The spacing dependence of the nonlocal spin signal at $T$ = 2 K, 10, and 80 K. The red dashed lines are the fitting curves based on spin superfluid model ( $R_{NL} \sim \frac{1}{d + L_\alpha}$ ), and the green dashed lines are fitting curves based on the incoherent magnon diffusion model ( $R_{NL} \sim \frac{1}{d}$ ). (**D**) The temperature dependence of $L_\alpha$ obtained based on the spin superfluid transport model.

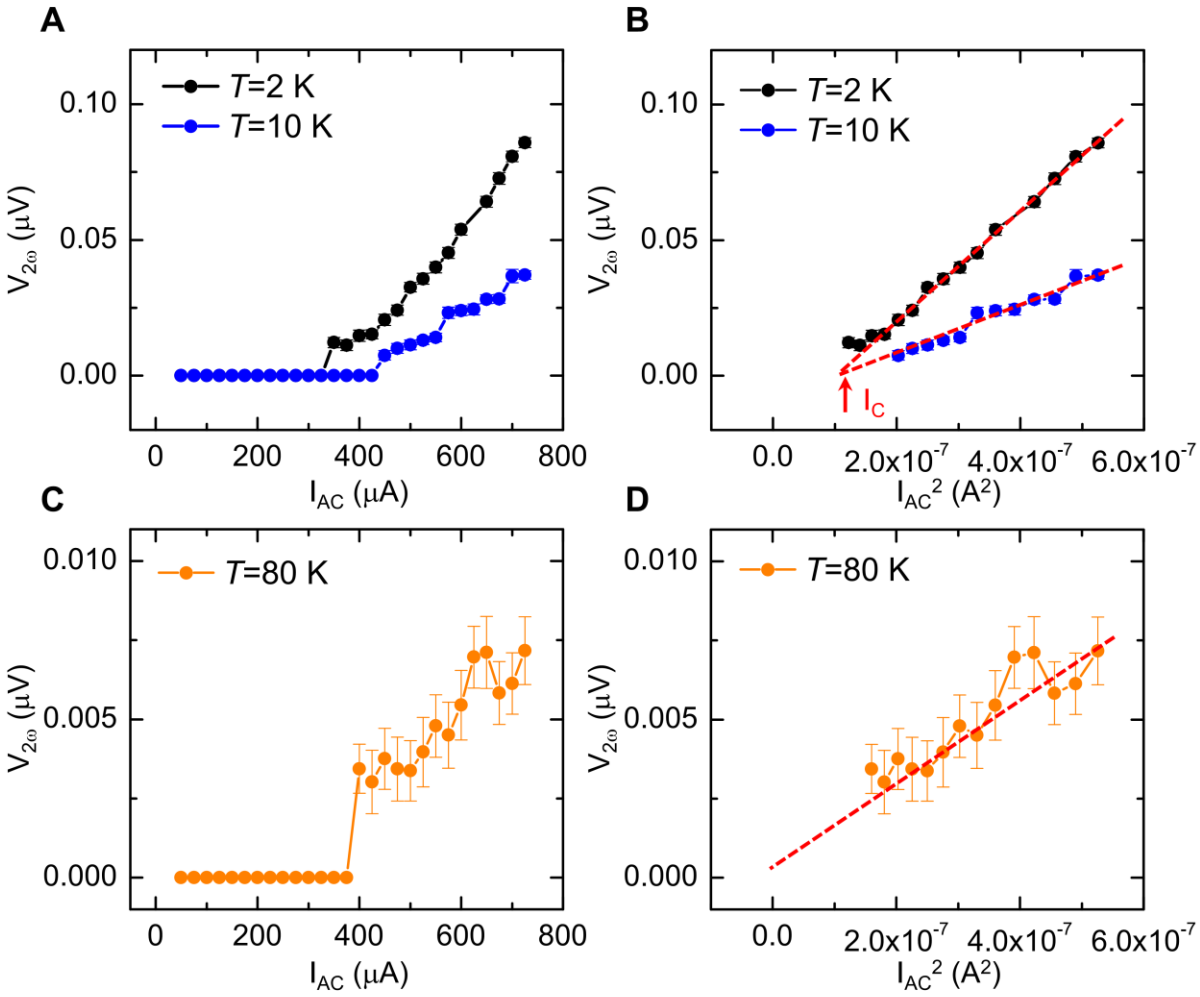


**fig. S14. Current dependence of the nonlocal spin transport on the ~18-nm (11$\bar{2}$0)-oriented $Cr_2O_3$ film.** (**A-B**) The second harmonic spin voltage vs. $I$ and $I^2$ at $T$ = 2 and 10 K and $B$ = 9 T on the device with $d$ = 10 μm. A critical current ($I_C$) is observed, which is needed to overcome uniaxial anisotropy to induce the spin superfluid transport. (**C-D**) The second harmonic spin voltage vs. $I$ and $I^2$ at $T$ = 80 K and $B$ = 9 T on the device with $d$ = 10 μm. The second harmonic voltage is proportional to $I^2$ without a critical current.

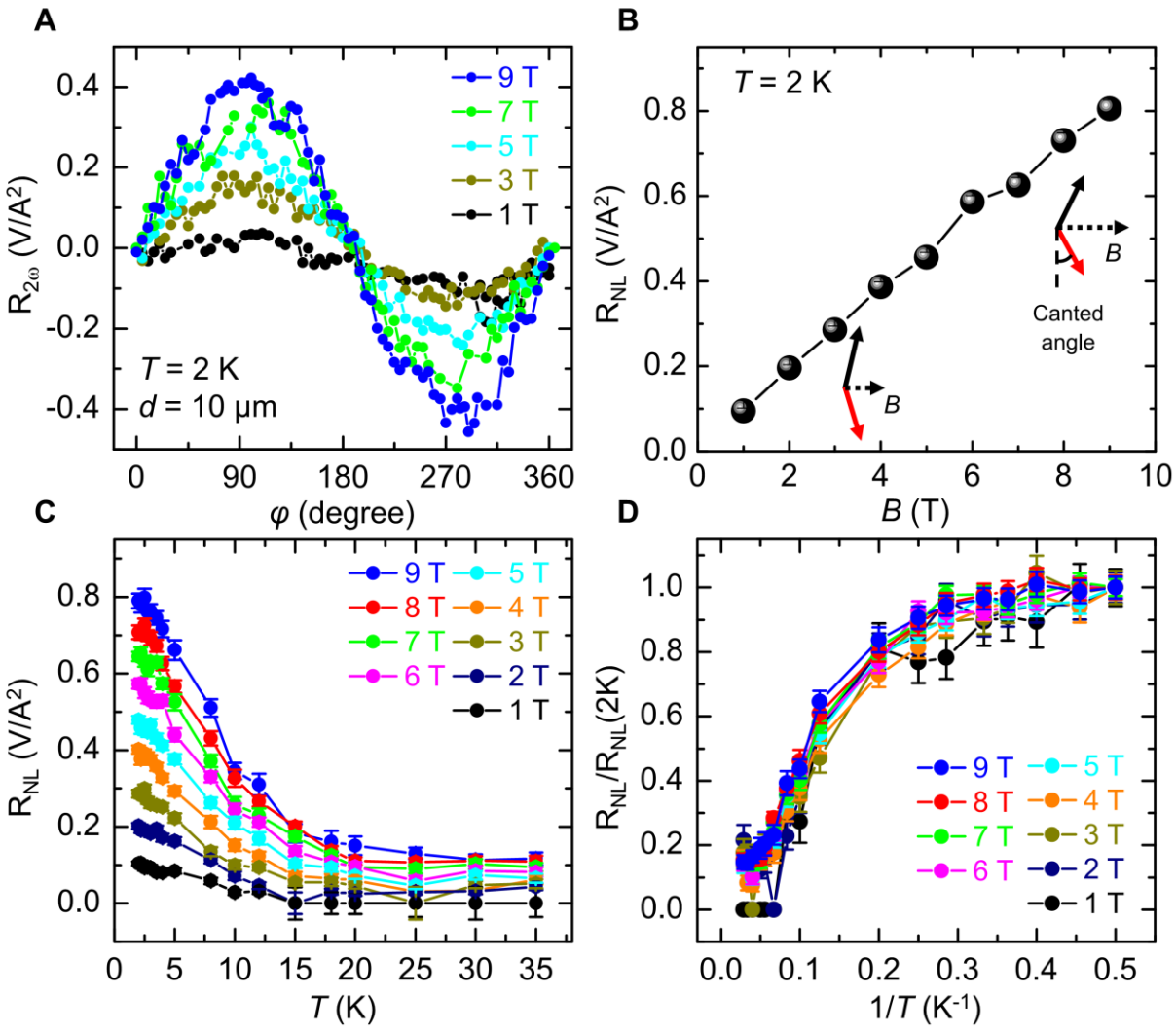


**fig. S15. Magnetic field dependence of nonlocal spin transport on the ~19-nm (0001)-oriented $Cr_2O_3$ film.** (**A**) The nonlocal second harmonic resistance as a function of the magnetic field angle at 2 K under the magnetic fields of 1 T, 3 T, 5 T, 7 T, and 9 T, respectively. (**B**) The nonlocal spin signal at 2 K as a function of the magnetic field. A larger magnetic field corresponds to a larger canted angle of the two antiferromagnetic spins. (**C**) The nonlocal spin signal as a function of the temperature under the magnetic fields from 1 T to 9 T. (**D**) The normalized nonlocal spin signal ( $R_{NL}$ / $R_{NL}$ (2K)) as a function of 1/*T* under the magnetic fields from 1 T to 9 T.